Chemical
Science

EDGE ARTICLE

View Article Online
View Journal | View Issue

Cite this: *Chem. Sci.*, 2025, **16**, 15499

Visible-light photoredox catalysis of polydopamine with triethanolamine in water†

Hoyun Kim,[a] Dokyeong Lee,[a] Young Jae Jung,[a] Sung Ho Yang,[b] Hye Jin Lee,[a] Hong-In Lee *[a] and Jungkyu K. Lee *[a]

Received 4th July 2025
Accepted 21st July 2025

DOI: 10.1039/d5sc04938e

rsc.li/chemical-science

Polydopamine (PDA), a synthetic melanin, has recently emerged as a photoreactive material, contrasting with its conventional role in photoprotection. In particular, its photochemical reactivity under visible light offers a new perspective on the role of melanin and opens up potential applications in biomedical engineering and energy conversion. However, the mechanism of the visible light-induced reactions is still not well understood, necessitating further systematic investigation. To address this challenge, we carefully investigated its photoredox catalysis under visible-light irradiation, focusing on electron transfer processes in the presence of triethanolamine as an electron donor. We explored various aspects, including its size-dependent reactivity, electrochemical and photophysical properties, and the characterization of generated radical species. Furthermore, we sought to optimize photoinitiated polymerization under various reaction conditions, such as different concentrations, monomers, and atmospheres. The use of water as a solvent is generally considered safe and poses minimal risk to human health and safety compared to many organic solvents. These results are crucial for advancing the understanding of melanin's photoredox catalytic mechanism and for developing innovative biocompatible photoreactive materials.

Introduction

Visible-light photoredox catalysts have been widely utilized in areas such as synthetic chemistry, energy conversion, phototherapy, and wastewater treatment because of their ability to efficiently harness visible light as a renewable source of chemical energy.[1–6] These catalysts enable chemical reactions to proceed under mild conditions, thereby minimizing undesirable side products and promoting environmentally friendly chemical processes.[7] By decreasing the reliance on harsh reagents and conditions, they foster more sustainable and green chemistry practices while also driving the development of novel synthetic methodologies.[8,9] Notably, organic photoredox catalysts have gained significant attention for their ability to expand the redox window and their applications in biomedical applications, such as phototherapy, cell encapsulation, and tissue engineering. This is largely due to their low cytotoxicity, structural flexibility, and compatibility with a wide range of functional groups.[10–16] These features make them ideal for biological systems, where decreasing toxicity is crucial, and their tunable structures allow them to be adapted for a wide range of biological environments and reactions. For example, visible-light photopolymerization initiated by organic photoredox catalysts has been used to encapsulate individual mammalian cells in polymeric shells, shielding them from environmental stresses and immunological attack while supporting cell survival and function.[11,12]

Recently, organic polymers have emerged as a promising alternative to small-molecule organic photoredox catalysts because of their facile synthesis and tunable optical and electronic properties.[17] These properties can be precisely adjusted by altering the monomer units or varying polymer chain lengths, making them highly versatile for a range of catalytic applications.[18–20] Among organic polymers, polydopamine (PDA), as a biomimetic polymer, is a promising photoredox catalyst due to its ease of formation both in solution and on surfaces, its abundance of functional groups, and its high molar absorptivity across a broad range of visible light.[21,22] Recently, Stenzel and coworkers demonstrated the effectiveness of PDA particles in dimethyl sulfoxide (DMSO) as a visible-light photoredox catalyst, highlighting its potential in this field.[23] The authors proposed that the initiation of the radical reaction resulted from a photoinduced electron transfer between diphenyliodonium (electron acceptor) and the semiquinone radical anion (SQR) (electron donor). Furthermore, the increased concentration of the SQR species was presumably

---

[a] Department of Chemistry, Green-Nano Materials Research Center, Kyungpook National University, Daegu 41566, South Korea. E-mail: jkl@knu.ac.kr; leehi@knu.ac.kr

[b] Department of Chemistry Education, Korea National University of Education, Cheongju 28173, South Korea

† Electronic supplementary information (ESI) available: Detailed experimental procedures, characterization and supporting figures. See DOI: https://doi.org/10.1039/d5sc04938e

caused by proton-coupled electron transfer (PCET) between 5,6-dihydroxyindole (QH_2) and 5,6-indolequinone (Q) units within the PDA particle under visible-light irradiation.[24,25]

However, a systematic investigation is still lacking, and further elucidation of the catalytic mechanism is essential for expanding its application across diverse areas.[26] In addition, investigating the photocatalytic efficacy of PDA in aqueous solution is crucial for its potential use in green chemistry, bioconjugation, and biological applications.[27,28] Herein, we investigate the photoredox catalysis of PDA in the presence of triethanolamine (TEOA), serving as an electron donor in water to obtain a better understanding of its catalytic mechanism under different reaction conditions. The photocatalytic efficacy of PDA is evaluated through radical polymerization, a method that enables efficient monitoring of catalyst activity while offering valuable insights into the underlying mechanism.[29] Compared with the prior work by Stenzel *et al.*, we employ an electron donor and thus propose a new mechanism involving PCET between the excited state of PDA and TEOA, supported by spectroscopic characterization (*e.g.*, time-resolved photoluminescence). In addition, conducting the reaction in water offers potential applications in areas such as chemobiosensors, cell encapsulation, and drug delivery systems.[30–34]

Results and discussion

Synthesis and characterization of water-soluble PDA particles

Dopamine hydrochloride (100 mg) was dissolved in 50 mL of a pH 11 buffer solution, and the pH gradually decreased to approximately 8.5 without the need for additional reagents. The solution was then shaken at 100 rpm for varying durations: 1 day (**PDA 1**), 15 days (**PDA 15**), 30 days (**PDA 30**) and 60 days (**PDA 60**). After the designated incubation periods, each solution was centrifuged at 1350 rpm for 1 min to remove the precipitated particles. The resulting supernatants were used as photoredox catalysts under visible light. The obtained PDA particles were initially characterized using FT-IR spectroscopy, UV-Vis spectrometry, and particle size analysis. The FT-IR spectrum was consistent with the literature, showing characteristic bands at 3200–3500 cm^{-1} (O–H and N–H stretching), 1475–1600 cm^{-1} (N–H bending and aromatic C═C stretching), and 1390 cm^{-1} (C–N stretching) (Fig. S1†).[35,36] The precise characterization of the PDA structure remains a topic of discussion due to its inherent complexities.[37] However, numerous studies suggest that PDA is primarily composed of QH_2, Q, and dopamine units (Fig. 1). These units are believed to be connected through both covalent bonds and non-covalent interactions, such as π–π stacking, cation–π interactions, and hydrogen bonding.[38,39]

Aqueous PDA solutions (0.022 w/v%) were transparent, indicating good water solubility (Fig. 2a). As the incubation time increased from **PDA 1** to **PDA 60**, the solution progressively darkened, indicating the formation of larger particles. Dynamic light scattering analysis confirmed this observation, revealing mean particle sizes of 132 (±61) nm, 165 (±17) nm, 240 (±96) nm, and 328 (±206) nm for **PDA 1, PDA 15, PDA 30,** and **PDA 60**, respectively (Fig. S2†). Zeta potential measurements were consistent with the particle size data, showing that larger particles generally exhibit higher stability: −17 (±12) mV for **PDA 1**, −14 (±15) mV for **PDA 15**, −37 (±7) mV for **PDA 30**, and −42 (±6) mV for **PDA 60**. UV-Vis spectra also revealed a positive correlation between absorbance in visible region and PDA particle size. For example, at a concentration of 0.022 w/v%, **PDA 60** and **PDA 30** showed absorbance values of 0.47 and 0.17 at 525 nm, respectively, whereas the other samples exhibited absorbance values of 0.08 at the same concentration (Fig. 2b). Even **PDA 60** demonstrated absorption in the near-infrared region.

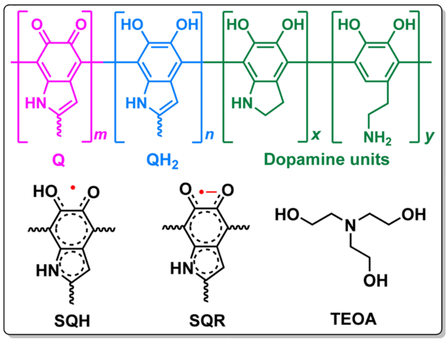

Fig. 1 Illustration of molecular structures of polydopamine (PDA), protonated semiquinone radical (SQH), semiquinone radical (SQR), and triethanolamine (TEOA).

Meanwhile, as the particle size increases, the λ_{max} of the absorption spectrum exhibits a blue-shift, progressively shifting from 406 nm (**PDA 1**) to 399 nm (**PDA 15**), 391 nm (**PDA 30**), and 380 nm (**PDA 60**) (Fig. S3†). In contrast, the emission spectrum shows a red-shift with increasing particle size. These opposing behaviors are characteristic of H-aggregate formation.[40,41]

Based on this, we assume that the growth of PDA with prolonged incubation time is primarily driven by non-covalent

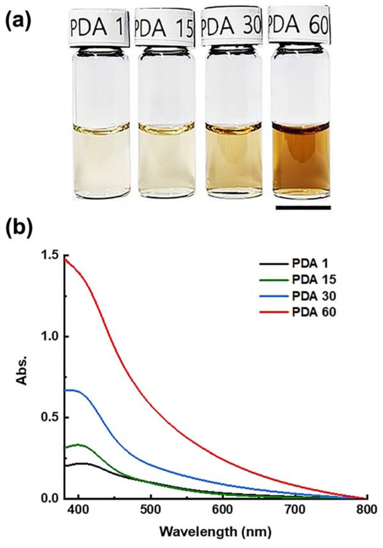

Fig. 2 (a) Representative images of the PDAs (0.022 w/v%) in water and (b) UV-Vis spectra of the PDAs (0.022 w/v%) in water. The scale bar indicates 1.5 cm.

Table 1 Investigation of photoinitiated free-radical polymerization of OEGMA in the presence of PDAs and TEOA under various conditions with green LED irradiation (520 ± 30 nm, 4.2 W cm^{-2})[a]

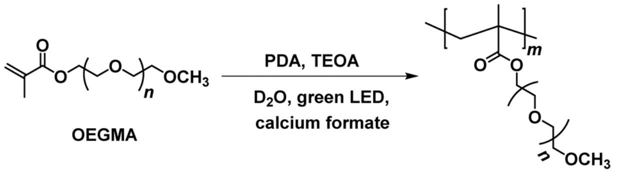

Entry	Type of PDA	Conc. of cat. (w/v%)	[OEGMA] : [TEOA] (mM)	Conversion[b] (%)	M_n[c] (kDa)	M_w/M_n	Atmosphere
1	**PDA 1**	0.022	500 : 50	0	<1	n.a.	Air
2	**PDA 15**	0.022	500 : 50	27 ± 7	635	3.93	Air
3	**PDA 30**	0.022	500 : 50	60 ± 11	≥767[d]	3–4	Air
4	**PDA 60**	0.022	500 : 50	98 ± 1	≥767	3–4	Air
5	**PDA 60**	0.0011	500 : 50	74 ± 4	≥767	3–4	Air
6	**PDA 60**	0.0055	500 : 50	93 ± 2	≥767	3–4	Air
7	**PDA 60**	0.011	500 : 50	96 ± 1	≥767	3–4	Air
8	**PDA 60**	0.044	500 : 50	70 ± 5	≥767	3–4	Air
9	**PDA 60**	0.088	500 : 50	51 ± 2	≥767	3–4	Air
10	**PDA 60**	0.11	500 : 50	21 ± 3	332	3.48	Air
11	None	0	500 : 50	0	<1	n.a.	Air
12	**PDA 60**	0.022	300 : 50	86 ± 10	≥767	3–4	Air
13	**PDA 60**	0.022	500 : 30	94 ± 1	≥767	3–4	Air
14	**PDA 60**	0.022	500 : 0	0	<1	n.a.	Air
15	**PDA 60**	0.022	500 : 50	96 ± 2	≥767	3–4	Ar
16	**PDA 60**	0.022	500 : 50	0	<1	n.a.	O_2
17	Fluorescein	0.022	500 : 50	89 ± 1	12	2.77	Air
18	Eosin Y	0.022	500 : 50	98 ± 1	11	1.73	Air

[a] Reactions were conducted for 3 h in a standard NMR tube sealed with a cap under aerobic conditions and in a J-Young NMR tube with a valve containing 0.5 mL of solution for Ar (g) and O_2 (g) atmospheres at room temperature. [b] Monomer conversions were determined by ^{1}H-NMR using calcium formate as an internal standard, as detailed in the ESI. Data were reported as mean ± standard deviation ($n = 3$). [c] Experimental molecular weights and polydispersity (M_w/M_n) were determined by GPC analysis using PMMA standards for calibration with DMF containing 1 mM LiBr as the eluent, as detailed in the ESI. [d] The upper detection limit. n.a.: not applicable.

interactions rather than covalent bonding, leading to an extended conjugated π-system.

Visible-light induced photopolymerization

Initially, we evaluated the photoredox catalytic performance of PDAs through photoinitiated, free-radical polymerization, exhibiting rapid reactivity. The photopolymerization of oligo(ethylene glycol) methyl ether methacrylate (OEGMA, 500 mM) was initiated using a green light-emitting diode (LED) (520 ± 30 nm, 4.2 W cm^{-2}) in aqueous solution, containing PDA (0.022 w/v%) and TEOA (50 mM) under aerobic conditions for 3 h (Table 1, entries 1–4). TEOA was chosen as a co-initiator due to its role as an electron donor. Our results showed a clear correlation between PDA size and polymerization efficiency: larger particles led to increased reactivity (Fig. 3a). Specifically, **PDA 60** exhibited superior vinyl conversion (98 ± 1%) and apparent first-order rate coefficient ($k_{app} = 4.7 \pm 0.1 \times 10^{-4}\ s^{-1}$) as determined by ^{1}H-NMR spectroscopy (Fig. S4 and S5a†). In contrast, **PDA 30** and **PDA 15** achieved vinyl conversions of 60 (±11)% and 27 (±7)%, respectively, with corresponding k_{app} values of 0.9 (±0.5) × 10^{-4} s^{-1} and 0.2 (±0.1) × 10^{-4} s^{-1}. **PDA 1** and the negative control (*i.e.*, without PDA) exhibited no vinyl conversion (Fig. S5a†). We assume that this trend can be affected by absorptivity in the visible-light region and the effectiveness of PDA as a free-radical inhibitor. For example, **PDA 60** exhibited a 2.7-fold higher absorbance value at 520 nm compared to **PDA 30** (Fig. 2b). In addition, the larger size of the PDA particle reduces their scavenging ability for free radicals due to the lower surface area-to-volume ratio.[42] After the photopolymerization, the formed polymers were characterized by gel permeation chromatography (GPC) with DMF containing 1 mM LiBr as an eluent. The number-average molecular weight (M_n) of the obtained polymers followed a similar trend to the vinyl conversion, with the maximum detectable M_n approximately 767 kDa (based on poly(methyl methacrylate) (PMMA) standards), limited by the viscosity of poly(OEGMA).

Given the superior performance of **PDA 60**, we further investigated its concentration effect in the presence of OEGMA (500 mM) and TEOA (50 mM) under visible-light irradiation for 3 h (Table 1, entries 5–10). Consistent with the previous report,[23] the polymerization rate increased with rising **PDA 60** concentration up to a certain point, after which it began to decline (Fig. 3b). For example, the vinyl conversions for 1.1 × 10^{-3} w/v% and 1.1 × 10^{-2} w/v% **PDA 60** were 74 (±4)% and 96 (±1)%, with corresponding k_{app} values of 0.7 (±0.2) × 10^{-4} s^{-1} and 3.6 (±0.2) × 10^{-4} s^{-1}, respectively (Fig. S5b†). However, at

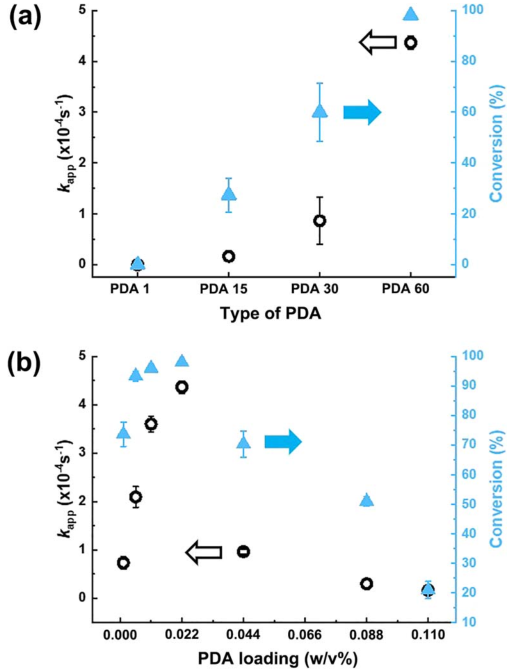

Fig. 3 Photoredox catalytic performance as a function of (a) PDA particle size and (b) concentration of **PDA 60**. k_{app}: apparent first-order rate coefficient.

concentrations exceeding 2.2×10^{-2} w/v%, the vinyl conversion rate decreased. For example, the vinyl conversions for 4.4×10^{-2} w/v% and 8.8×10^{-2} w/v% **PDA 60** were 70 (±5)% and 51 (±2)%, with corresponding k_{app} values of $0.9\ (\pm 0.1) \times 10^{-4}\ s^{-1}$ and $0.3\ (\pm 0.2) \times 10^{-4}\ s^{-1}$, respectively. This result can be attributed to the reduced light penetration at higher PDA concentrations.[23] As the concentration of **PDA 60** increased, we observed a corresponding decrease in penetration depth (Table S1†). Furthermore, we assume that higher PDA concentrations increase the concentration of radical species, which in turn promotes radical termination. As a negative control, we could not observe the vinyl conversion in the absence of **PDA 60** (Table 1, entry 11). Consequently, the optimal concentration of **PDA 60** is required for efficient photopolymerization.

We examined the concentration effect of OEGMA and TEOA for the photopolymerization with **PDA 60** (0.022 w/v%) under the visible-light irradiation for 3 h (Table 1, entries 12–14). Typically, as their concentrations increased, the vinyl conversion and k_{app} value increased. For example, 500 mM of OEGMA exhibited 2 times higher vinyl conversion rate than 300 mM of OEGMA ($k_{app} = 1.6 \pm 0.1 \times 10^{-4}\ s^{-1}$) in the presence of **PDA 60** and TEOA (50 mM) (Fig. S6a†). Furthermore, 50 mM of TEOA showed a slightly higher vinyl conversion rate ($k_{app} = 4.7 \pm 0.1 \times 10^{-4}\ s^{-1}$) of OEGMA (500 mM) than 30 mM of TEOA ($k_{app} = 3.7 \pm 0.2 \times 10^{-4}\ s^{-1}$) with **PDA 60** (Fig. S6b†). As a negative control, no vinyl conversion was observed in the absence of TEOA after 3 h. Taken together, the suitable concentrations for the photopolymerization were approximately 0.022 w/v% of **PDA 60**, 500 mM of OEGMA, and 50 mM of TEOA. As a negative control, no vinyl conversion was observed under these optimized reaction conditions in the absence of visible-light irradiation, even after 100 days under ambient conditions (Fig. S7†).

Under optimized concentration conditions, we also conducted the photocatalysis of **PDA 60** in different atmospheres. In an argon (g) atmosphere, the photopolymerization rate was slightly faster than that observed under an aerobic atmosphere (Fig. 4a, blue line). For example, vinyl conversion at 10 min was nine times greater in the argon atmosphere (Table 1, entries 15 and 16). This result suggests that PDA-based photoredox catalysis is inhibited by molecular oxygen, unlike the eosin Y-based system, where molecular oxygen facilitates the regeneration of the dye.[43] To confirm this, we carried out the reaction under an O_2 (g) atmosphere. As a result, no vinyl conversion was observed under continuous O_2 (g) purging conditions (Fig. 4a, red line). However, when O_2 (g) was supplied once for 1 h without continuous purging, vinyl conversion occurred after an initial delay. Specifically, no conversion was observed during the first 1.5 h of irradiation; however, after 6 h, the conversion reached 96% (Fig. 4a, green line).

The significant suppression of the reaction in the presence of oxygen indicates the scavenging activity of molecular oxygen. We assume that PDA mediates the conversion of molecular oxygen to hydrogen peroxides under both dark and irradiation conditions. Thus, the generated reactive oxygen species inhibit the radical reactions until the available oxygen is consumed.[44] In addition, the introduction of excess oxygen led to a decrease in the photocatalytic performance of PDA, consistent with the

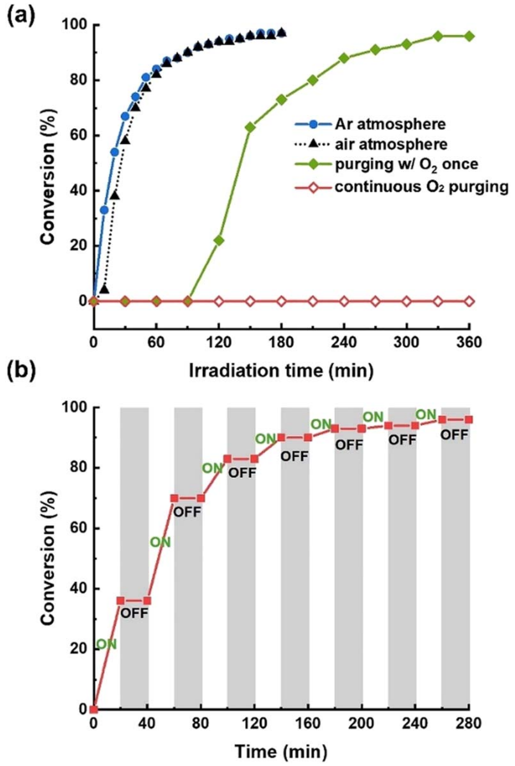

Fig. 4 PDA-based photoredox catalysis (a) under different atmospheric conditions and (b) with temporal light control.

Table 2 Monomer scope and optimization in the PDA/TEOA system under aerobic conditions with green LED irradiation[a]

Entry	Monomer	Additive (conc. mM)	Conversion[b] (%)	M_n[c] (kDa)	M_w/M_n
1	MA	None	5	<1	n.a.
2	HEMA	None	5	<1	n.a.
3	NIPAm	None	<1	<1	n.a.
4	MEDSAH	None	71	≥767[d]	3–4
5	HEMA	PEG_{400} (50)	5	<1	n.a.
6	HEMA	PEG_{400} (100)	60	163	3.51
7	HEMA	PEG_{400} (250)	74	214	2.58
8	HEMA	Glycerol (250)	6	<1	n.a.
9	HEMA	Glycerol (400)	61	202	3.56
10	NIPAm	PEG_{400} (250)	44	156	4.08
11	MA	PEG_{400} (250)	18	<1	n.a.

[a] Reactions were conducted for 3 h in a standard NMR tube sealed with a cap, containing 0.5 mL of a solution of **PDA 60** (0.022 w/v%), monomer (0.5 M), and TEOA (50 mM) dissolved in D_2O under aerobic conditions at room temperature. [b] Monomer conversions were determined by ^{1}H-NMR using calcium formate as an internal standard. [c] Experimental molecular weights and polydispersity (M_w/M_n) were determined by GPC analysis using PMMA standards for calibration with DMF containing 1 mM LiBr as the eluent. [d] The upper detection limit. MA: methacrylic acid, HEMA: 2-hydroxyethyl methacrylate, NIPAm: *N*-isopropylacrylamide, MEDSAH: [2-(methacryloyloxy)ethyl]dimethyl-(3-sulfopropyl)ammonium hydroxide, and PEG: poly(ethylene glycol).

PDA oxidation observed in photobleaching experiments detailed below. Meanwhile, excellent temporal control in the photopolymerization process was demonstrated through light "ON" and "OFF" experiments at 20 min intervals (Fig. 4b). During the cycles, the vinyl conversion occurred under visible-light irradiation, whereas no vinyl conversion was observed in the absence of the irradiation.

We also compared the photoredox catalytic performance of PDA with that of fluorescein and eosin Y, both well-known organic photoredox catalysts (Fig. S8†). Under the identical reaction conditions, fluorescein exhibited lower photocatalytic efficacy than **PDA 60**. For example, the monomer conversion reached 89 (±1)%, with a corresponding k_{app} value of 1.9 (±0.1) $\times 10^{-4}$ s^{-1} and M_n of 12 kDa ($M_w/M_n = 2.77$) (Table 1, entry 17). Eosin Y showed a photocatalytic efficacy comparable to **PDA 60**, achieving a monomer conversion of 98 (±1)%, k_{app} value of 4.4 (±0.3) $\times 10^{-4}$ s^{-1}, and M_n of 11 kDa ($M_w/M_n = 1.73$) (Table 1, entry 18). The relatively low M_n values are attributed to the high concentrations of the dyes.

We determined the reaction quantum yield of this photopolymerization. The quantum yield (Φ) of a photochemical reaction is defined as the ratio of the number of products formed ($N_{products}$) to the number of photons absorbed at a specific wavelength ($N_{photons}$, abs(λ)).[45] To determine the number of $N_{products}$, we measured the monomer conversion using ^{1}H-NMR spectroscopy. The experiment was performed under the conditions described in Table 1, entry 4, and yielded a monomer conversion of 3% after 60 s of irradiation. The corresponding value of $N_{products}$ was calculated to be 0.015 M. The value of $N_{photons}$ was calculated based on our previous report.[46] Accordingly, the calculated value of the $N_{photons}$ was 0.013 M. Thus, the quantum yield of the photopolymerization was 1.15.

We also determined the kinetic chain length (ν = propagation rate (R_p)/initiation rate (R_i)) of **PDA 60**. The R_p value was obtained from polymerization kinetics measured by ^{1}H-NMR spectroscopy. Based on triplicate experiments under the conditions described in Table 1, entry 4, the R_p value was calculated to be 6.0 (±0.6) $\times 10^{-2}$ M s^{-1} (Fig. S9†). The R_i value was determined using a previously reported method.[47] Briefly, the R_i value refers to the average initiation rate during the inhibition period of **PDA 60**. The concentration of 2,2,6,6-tetramethylpiperidine-1-oxyl (TEMPO), used as a radical inhibitor, was plotted against inhibition time (t_{inh}). The R_i value was calculated as the inverse slope of the resulting line ([TEMPO]/t_{inh}) and was found to be 3.5 (±0.3) $\times 10^{-5}$ M s^{-1} (Fig. S9†). Accordingly, the kinetic chain length was calculated to be 1727 (±86), which is similar to the M_n value measured by GPC.

To expand the monomer scope, we investigated the polymerization of various water-soluble monomers under the optimized conditions as shown in Table 2. Our findings reveal a strong correlation between the molecular weight of the monomer and its vinyl conversion. Monomers with a relatively high molecular weight exhibited significantly higher conversion rates compared to those with a low molecular weight. For example, methacrylic acid (MA), 2-hydroxyethyl methacrylate (HEMA), and *N*-isopropylacrylamide (NIPAm) displayed vinyl conversions below 5%, while [3-(methacryloyloxy)ethyl] dimethyl-(3-sulfopropyl)ammonium hydroxide (MEDSAH) achieved 71% conversion after 3 h of irradiation (Table 2, entries 1–4). We assume that viscosity plays a key role in these results, given that PDA acts as an inhibitor. As the viscosity of the solution increases, the termination rate of polymerization decreases (*i.e.*, Trommsdorff effect).[48] To test this assumption, we introduced poly(ethylene glycol) (M_n = 400 Da, PEG_{400}) as a viscosity-enhancing agent. As expected, PEG_{400} significantly improved the conversion of low-molecular-weight monomers. For example, the vinyl conversion of HEMA increased from negligible levels to 60% (M_n = 163 kDa) and 73% (M_n = 214 kDa) with 100 mM and 250 mM of PEG_{400}, respectively (Table 2, entries 5–7, Fig. S10†). To further confirm the effect of viscosity, glycerol was used as an alternative to PEG (Table 2, entries 8 and 9). The vinyl conversion of HEMA reached 61% (M_n = 202 kDa) at a glycerol concentration of 400 mM (Fig. S10†). Furthermore,

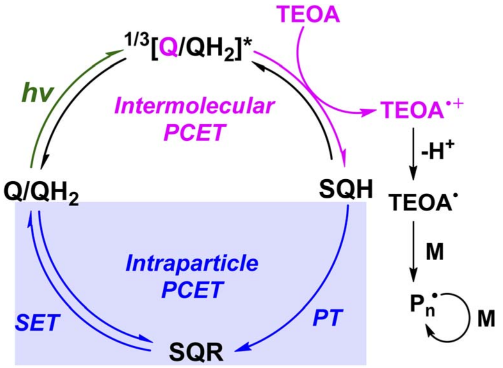

Scheme 1 Plausible mechanism of photoredox catalysis of polydopamine (aq) under visible-light irradiation. PCET: proton-coupled electron transfer; PT: proton transfer; SET: single-electron transfer.

the vinyl conversion of NIPAm increased significantly to 44% in the presence of 250 mM PEG$_{400}$ (Table 2, entry 10). In contrast, the vinyl conversion of MA showed only a modest increase to 18% with PEG$_{400}$ (250 mM), presumably due to a pH effect (Table 2, entry 11). The excess amount of MA can convert TEOA to a quaternary ammonium salt, thereby hindering the single-electron transfer (SET) between TEOA and the PDA.

Plausible mechanism

Based on our results, we propose the following photoredox catalytic pathway. Upon exposure to visible light, a PDA chain – composed predominantly of covalently bonded QH$_2$ and Q units – transitions to a singlet or triplet excited state, denoted as $^{1/3}$[Q/QH$_2$]*. In the presence of an electron donor such as TEOA, a protonated semiquinone radical (SQH) is generated through proton-coupled electron transfer (PCET) between $^{1/3}$[Q/QH$_2$]* and TEOA (*i.e.*, intermolecular PCET) (Scheme 1). In this process, the excited Q species accepts an electron from the excess TEOA. Subsequently, the SQH species rapidly loses a proton to form a semiquinone radical anion (SQR), which is stabilized by the negative charge on its conjugate base.[49] However, our investigation of monomer conversion under dark conditions suggested that this SQR, which also forms in the absence of light,[24] rarely initiates radical reactions in this system. The SQR then returns to [Q/QH$_2$] through SET. These two sequential steps are collectively referred to as intraparticle PCET. Following the intermolecular PCET, TEOA generates an α-amino radical by first forming an amino radical cation, which subsequently undergoes proton abstraction, thereby initiating radical reactions.

Analysis using electron paramagnetic resonance (EPR) spectroscopy

It has been reported that several radical species are involved in the photoreactions of melanin-based compounds.[23,24,50,51] EPR spectroscopy was employed to track the radical species generated during the photoreaction of PDA. Fig. 5a and b show the EPR spectra of aqueous **PDA 60** (0.55 w/v% in water) solutions under dark conditions and after 10 minutes of visible-light irradiation, respectively. In both the spectra, broad EPR signals *ca.* $g = 2.0040–2.0050$ were observed. These can be assigned to carbon-based radical (CCR) or SQR of PDA.[23,24,51,52] And it is noticed that the visible-light irradiation increased the signal intensity.

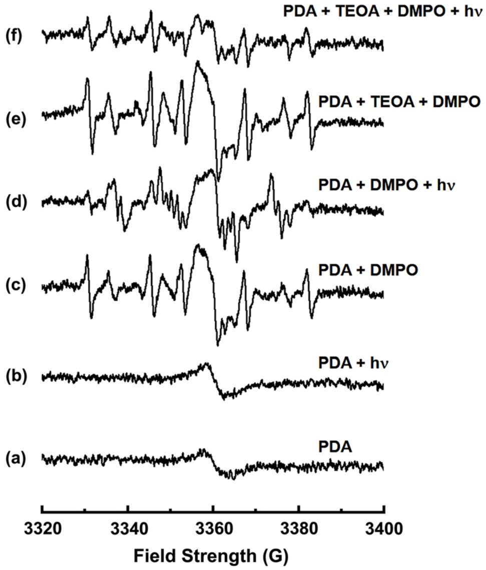

Fig. 5 Solution EPR spectra obtained from aqueous solutions of **PDA 60** + TEOA + DMPO at room temperature under visible-light irradiation: (a) **PDA 60** in water, (b) **PDA 60** + *hν* in water, (c) **PDA 60** + DMPO in 70% aqueous DMSO, (d) **PDA 60** + DMPO + *hν* in 70% aqueous DMSO, (e) **PDA 60** + DMPO + TEOA in 70% aqueous DMSO, and (f) **PDA 60** + DMPO + TEOA + *hν* in 70% aqueous DMSO. Experimental conditions: microwave frequency, 9.413–9.427 GHz; microwave power, 6.32 mW; modulation amplitude, 1.00 G; modulation frequency, 100 kHz; time constant, 0.08192 s; and [**PDA 60**] = 0.55 w/v%, [TEOA] = 0.1 M, and [DMPO] = 0.1 M.

To detect open-shell species such as oxygen- and carbon-centered radicals, generated during the photoreaction of PDA, we adapted spin-trap EPR spectroscopy using 5,5-dimethyl-1-pyrroline-*N*-oxide (DMPO) as a spin trap. DMPO is particularly effective for characterizing these unstable radical intermediates, as its spin adducts exhibit distinctive EPR parameters. Fig. 5c–f display the spin-trap EPR spectra obtained from the aqueous **PDA 60** solutions containing 0.1 M DMPO either with or without 0.1 M TEOA and either after 10 minutes of visible-light irradiation or dark conditions. 70% aqueous DMSO was used to prepare DMPO-containing samples for ensuring adequate solubility. We observed that DMPO adducts were decomposed and/or rearranged under the irradiation conditions.[52,53] To minimize the degradation of the DMPO adducts, each sample in a vial was irradiated with a green LED for 10 min prior to the addition of DMPO to the solution. After adding DMPO, the samples were stirred under dark conditions for 30 min before EPR measurements to ensure sufficient reaction. The visible-light irradiation of the samples was conducted outside the equipment.

Comprehensive simulations on the spin-trap EPR spectra (Fig. 5c–f) found six radical species; CCR, SQR, DMPO–C*, DMPO–OH, N*, and DMPO–OPh (Fig. 6). Their EPR simulation parameters are listed in Table 3. Comparing the simulated spectra before and after the irradiation, two distinctive changes are noticed. One is the increase of the SQR signal intensity by visible light. This is presumably due to the light-induced PCET process.[23] Most importantly, the EPR spectra of PDA + DMPO and PDA + DMPO + TEOA solutions after irradiation exhibited distinctive EPR signals corresponding to the DMPO–OPh adduct with $g = 2.0068$, $A(\mathrm{N}) = 13.2$ G, $A(\mathrm{H}_\beta) = 10.4$, and $A(\mathrm{H}_\gamma) = 1.4$ G.[50] These signals were absent before the irradiation. We assume that the light-induced PCET generated SQH species, which was subsequently trapped by DMPO. These findings support the light-induced mechanism in PDA-based photoredox catalysis.

In the case of DMPO–OH, PDA can generate hydrogen peroxides even in the absence of the irradiation under an aerobic atmosphere.[44] To verify this, we conducted quantitative analysis of hydrogen peroxide production using a colorimetric method with *N*,*N*-diethyl-*p*-phenylenediamine sulfate (DPD) and peroxidase (POD) (ESI†).[54] After 10 min of irradiation, hydrogen peroxide concentrations were 6.7 μM in an oxygen-rich atmosphere and 5.5 μM in an ambient atmosphere (Fig. S11†). We assume this difference to the varying oxygen concentrations in the samples. In the absence of the irradiation, hydrogen peroxide was generated at a consistent concentration of 4 μM regardless of the atmosphere. We assume that the comproportionation equilibrium between Q and QH_2 accounts for hydrogen peroxide generation without employing irradiation. The resulting hydrogen peroxide is subsequently converted into hydroxyl radicals.[63]

Table 3 EPR simulation parameters for the spectra shown in Fig. 5

Radicals	g_{iso}	Hyperfine coupling constants (G)			Peak-to-peak linewidths (G)
		N	H_β	H_γ	
DMPO–OPh[52]	2.0068	13.2	10.4	1.4	1.1
N*[a]	2.0066	13.9	—	—	1.5
DMPO–OH[b] (ref. 55–57)	2.0066	14.2	12.7	—	1.3
DMPO–C*[c] (ref. 58–61)	2.0065	14.8	21.9	—	1.0
SQR[23,24,50,51]	2.0044	—	—	—	3.5
CCR[23,24,50,51]	2.0049	—	—	—	6.0

[a] This signal might be attributed to the degradation of DMPO. [b] We assume that the redox reaction (comproportionation equilibrium) is responsible for hydrogen peroxide generation, subsequently converted into hydroxyl radicals. [c] The hyperfine coupling constants are close to the values found from the DMPO spin adduct of carbon-based radicals (*e.g.*, methyl radicals and the defect sites of the PDA backbone (*Ndef*')).[51,62]

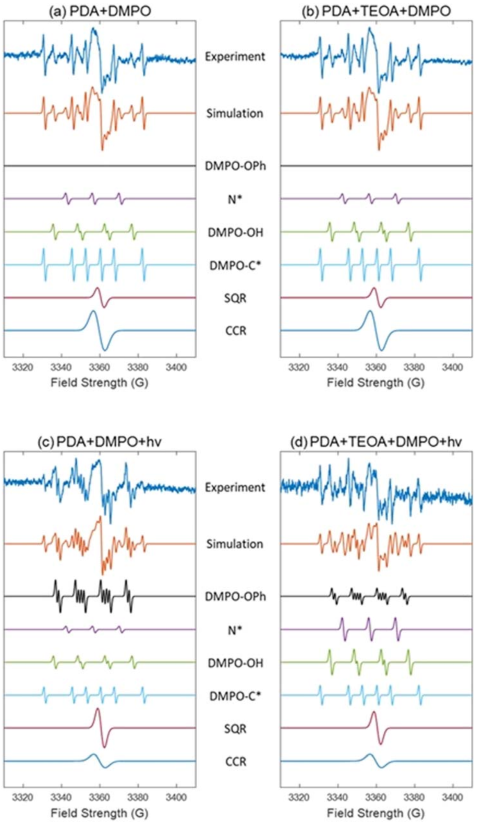

Fig. 6 EPR spectra obtained from aqueous solutions, along with their corresponding numerical simulations, for (a) **PDA 60** + DMPO, (b) **PDA 60** + TEOA + DMPO, (c) **PDA 60** + DMPO + *hν*, and (d) **PDA 60** + TEOA + DMPO + *hν*. The experimental spectra are the same as in Fig. 5. The simulated spectra are the sum of the individual spectra shown in Table 3.

The hyperfine coupling constants are close to the values found from the DMPO spin adduct of carbon-based radicals. Two possibilities are suggested for the signal. DMSO can be decomposed by the hydroxyl radical, generating methyl radicals that subsequently form DMPO–CH_3.[62] Other possibility is that DMPO forms spin adducts with the defect sites of the PDA backbone (*Ndef*').[51]

Analysis using time-resolved photoluminescence and electrochemical potentials

We also characterized the photophysical and electrochemical properties of the PDAs to support the photoinduced electron transfer (PET) between the PDA and TEOA (Table 4). According to the literature, photoreactions of melanin, which has a structure similar to that of PDA, occur *via* its triplet excited state.[64] Thus, we assume that the triplet excited state of PDA primarily involved in the PET process. **PDA 1** exhibited insufficient emission intensity for time-resolved photoluminescence measurements (FLS1000, Edinburgh Instruments Ltd, UK). As the size of PDA (aq) increased, the emission bands showed a red shift (Fig. S3†). At 77 K, phosphorescence was observed for **PDA 30** and **PDA 60**, while **PDA 15** showed no such emission. The phosphorescence maximum wavelengths (λ_P) were 544 nm for **PDA 60** and 514 nm for **PDA 30**, with corresponding lifetimes of 0.8 (±0.2) ms and 0.4 (±0.3) ms, respectively (Fig. 7a, b, S12 and S13†). Furthermore, **PDA 60** exhibited higher phosphorescence intensity than **PDA 30** under identical conditions, suggesting a higher triplet quantum yield for **PDA 60** (Fig. 7a). This result likely accounts for the superior photoredox catalytic performance of **PDA 60**. Based on the λ_P values, the triplet excited state energies ($E_{0,0}^{\mathrm{T1}}$) were determined to be 2.41 eV for **PDA 30** and

Table 4 Summary of photophysical and electrochemical properties of PDAs[a]

Substrate	PDA 15	PDA 30	PDA 60
$\lambda_{\mathrm{ex,vis}}$ (nm)	396	392	379
$\lambda_{\mathrm{F,vis}}$ (nm)	477	482	483
τ_{F} (ns)	2.8 (±0.2, 73%) 6.0 (±0.4, 27%)	2.2 (±0.5, 79%) 9.4 (±0.3, 21%)	3.7 (±0.3, 73%) 10.8 (±0.4, 27%)
λ_{P} (nm)	n.a.	514	544
τ_{P} (ms)	n.a.	0.4 (±0.3, 85%) 5.3 (±5, 15%)	0.8 (±0.2, 84%) 6.3 (±3, 16%)
$E_{1/2}^{\mathrm{red}}$ (V/SCE)[b]	−0.59	−0.67	−0.69
$E_{0,0}^{\mathrm{T1}}$ (eV)[c]	n.a.	2.41	2.28
ΔG_{PET} (eV)[d]	n.a.	−0.89	−0.73

[a] Determined in aqueous solution containing PDA (0.022 w/v%). [b] Determined in pH 11 buffer (aq) containing PDA (0.011 w/v%). [c] Determined under cryogenic conditions. [d] $\Delta G_{\mathrm{PET}} = -[E_{\mathrm{red}}^{*}(\mathrm{dye}^{*}/\mathrm{dye}^{\cdot-}) - E_{\mathrm{ox}}(\mathrm{TEOA}^{\cdot+}/\mathrm{TEOA})]$, $E_{\mathrm{red}}^{*}(\mathrm{dye}^{*}/\mathrm{dye}^{\cdot}) = E_{\mathrm{red}}(\mathrm{dye}/\mathrm{dye}^{\cdot-}) + E_{0,0}^{\mathrm{T1}}$, and $E_{\mathrm{ox}}(\mathrm{TEOA}^{\cdot+}/\mathrm{TEOA}) = 0.86$ eV, which was determined in 1 mM NaOH (aq.).

2.28 eV for **PDA 60**. Furthermore, the fluorescence lifetimes at room temperature were measured as 2.8 (±0.2) ns for **PDA 15**, 2.2 (±0.5) ns for **PDA 30**, and 3.7 (±0.3) ns for **PDA 60** (Fig. 7c, S12 and S14†).

In the presence of TEOA, we observed a 100-fold increase in the phosphorescence lifetime of **PDA 60**, reaching 82 (±16) ms (Fig. S13c†). This observation is consistent with previous reports demonstrating that electron donation can significantly enhance the phosphorescence lifetime.[65] This effect is presumably due to weakened vibrational relaxation of the triplet excited state and facilitated intermolecular interactions that reduce non-radiative relaxation.[66] In contrast, the fluorescence lifetime of the PDA remained largely unchanged in the presence of TEOA (Fig. S14†). These results suggest a mechanism of photoinduced electron transfer between TEOA and the triplet excited state of the PDA as shown in Scheme 1.

We determined the reduction potential of PDAs and the oxidation potential of TEOA (0.86 eV) using linear sweep voltammetry analysis (Fig. S15†). As a result, the reduction potential increased with increasing PDA size, with values of −0.59 for **PDA 15**, −0.67 eV for **PDA 30**, and −0.69 for **PDA 60**. With these experimental results, we were able to determine the Gibbs free energy of the photoinduced electron transfer (ΔG_{PET}). ΔG_{PET} represents the driving force for the intermolecular electron transfer between the PDA and TEOA, based on Marcus theory. According to the theory, the rate constants for electron transfer increase with increasing $-\Delta G^{\circ}$ values until reaching a maximum, and then decrease in the inverted region. The ΔG_{PET} values for **PDA 30** and **PDA 60** were −0.89 eV and −0.73 eV, respectively. These values suggest that the PET between the PDAs and TEOA is a spontaneous reaction. Based on the literature on photoredox catalysis using TEOA, we assume that these large negative ΔG_{PET} values fall within the inverted region. Kinetically, we believe that **PDA 60** exhibits a superior rate constant for the electron transfer compared to the other PDAs. Consequently, **PDA 60** demonstrated superior properties, including absorptivity in the visible range, triplet quantum yield, and electron transfer rate, contributing to its enhanced photoredox catalytic performance.

Photobleaching of PDA

The photobleaching of PDA is primarily attributed to its irreversible oxidation, ultimately leading to oxidative degradation.[67] Thus, photochemical reactions involving PDA can significantly

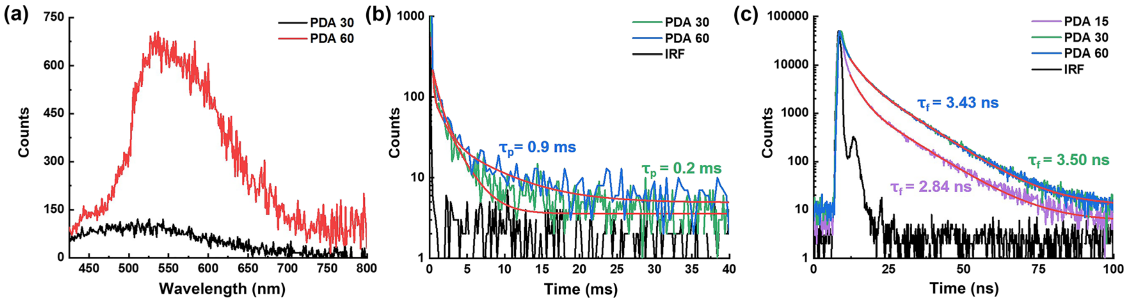

Fig. 7 Photoluminescence profiles of PDAs in water. (a) Time-gated phosphorescence spectra of **PDA 30** (black line) and **PDA 60** (red line) at 77 K with a delay time of 0.8 ms. (b) Phosphorescence decay profiles of **PDA 30** (green line) and **PDA 60** (blue line) at 77 K. Red lines represent the best-fit curves, and the black line indicates the instrument response function (IRF). (c) Fluorescence decay profiles of **PDA 15** (purple line), **PDA 30** (green line), and **PDA 60** (blue line) at room temperature. Red lines represent the best-fit curves, and the black line indicates the instrument response function (IRF).

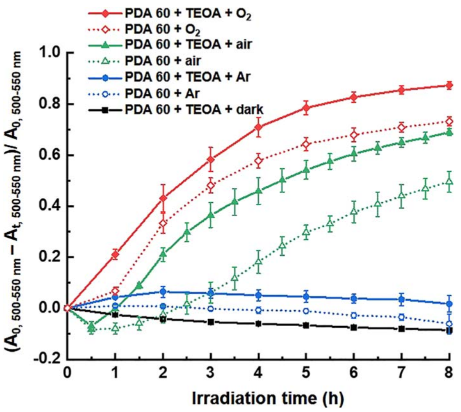

Fig. 8 Photobleaching of **PDA 60** under different conditions.

influence its oxidation rate. To further support our proposed photocatalytic mechanism, we examined the photobleaching behavior of PDA under different conditions such as different atmospheres. The degree of photobleaching was evaluated by monitoring the change in the summed absorbance values of **PDA 60** (0.022 w/v%) within the 500–550 nm range, corresponding to the wavelength of the LED light source, over time under the irradiation (Fig. 8). Under aerobic conditions with TEOA present, no photobleaching of the PDA was observed in a dark room (black solid line), whereas 70% photobleaching occurred after 8 h of irradiation (green solid line). Without TEOA, photobleaching of **PDA 60** was still substantial (50%) (green dotted line). However, under an argon atmosphere, the photobleaching was nearly negligible, and TEOA slightly increased photobleaching (blue lines). These results indicate that oxygen mainly contributes to photobleaching. To further confirm the role of oxygen, the photobleaching study was conducted under an oxygen atmosphere (red lines). As a result, photobleaching of PDA increased by 20% compared to aerobic conditions (red solid line). These results highlight the crucial role of oxygen in PDA photobleaching, which ultimately diminishes its photocatalytic performance. Furthermore, the presence of TEOA increased photobleaching under both air and oxygen atmospheres. This result is assumed to result from the interactions between PDA and TEOA, such as intermolecular PCET.

Conclusions

In addition to its biocompatible and adhesive properties, polydopamine serves as a visible-light photoredox catalyst, enabling photochemical reactions in aqueous solutions under mild reaction conditions. The photoredox catalytic performance of polydopamine particles (PDAs) of various sizes was systematically investigated through photoinitiated radical polymerization. Our findings demonstrate that PDAs act as electron acceptors in the presence of TEOA under visible-light irradiation and are regenerated *via* PCET, progressing through SQH and SQR intermediates. The SQH species was characterized using EPR spectroscopy with a spin-trapping agent. Upon the intermolecular PCET, TEOA first forms an amino radical cation, which subsequently undergoes proton abstraction to generate an α-amino radical, thereby initiating radical reactions. Notably, larger PDAs exhibited superior photoredox catalytic performances. For example, **PDA 60** showed higher absorptivity and phosphorescence intensity in the visible-light range than the smaller ones. Additionally, its more red-shifted emission, leading to a lower triplet state energy, resulted in a less negative ΔG_{PET} value relative to the others. The combination of this finding and the electrochemical analysis of the PDA and TEOA provides evidence that the triplet excited state of PDA is favorable for the PET process.

Furthermore, the photobleaching study of **PDA 60** supports the proposed photocatalytic mechanism. Our investigation exhibited that light irradiation and molecular oxygen play crucial roles in the photobleaching process. In the absence of oxygen, the photobleaching of PDA was nearly negligible, even in the presence of light irradiation and TEOA, suggesting that the photoredox catalysis of PDA is more favorable under an inert atmosphere. Additionally, no photobleaching was observed in a dark room even with oxygen and TEOA present, which corresponded to no monomer conversion. These findings indicate the light selectivity of the PDA/TEOA system. TEOA was found to increase the extent of PDA photobleaching under the bleaching conditions, presumably due to the intermolecular PCET between TEOA and PDA. We envision that these experimental results of visible-light photoredox catalysis with PDA will help elucidate its mechanism and play a key role in exploiting the diverse optoelectronic applications of melanin derivatives.

Data availability

The data supporting this article have been included as part of the ESI.†

Author contributions

The manuscript was written through contributions of all authors. All authors have given approval to the final version of the manuscript.

Conflicts of interest

There are no conflicts to declare.

Acknowledgements

This research was supported by the National Research Foundation of Korea (NRF) grant funded by the Korea government (MSIT) (RS-2023-00239038).

Notes and references

1 A. Blázquez-Moraleja, O. Cabezuelo, R. Martinez-Haya, L. C. Schmidt, F. Bosca and M. L. Marin, *Pure Appl. Chem.*, 2023, **95**, 899–912.

2 D. A. Nicewicz and D. W. C. MacMillan, *Science*, 2008, **322**, 77–80.

3 Y. O. Wang, A. Vogel, M. Sachs, R. S. Sprick, L. Wilbraham, S. J. A. Moniz, R. Godin, M. A. Zwijnenburg, J. R. Durrant, A. I. Cooper and J. W. Tang, *Nat. Energy*, 2019, **4**, 746–760.

4 A. Pavanello, M. A. Miranda and M. Marin, *Chem. Eng. J. Adv.*, 2022, **11**, 100296.

5 B. S. Howerton, D. K. Heidary and E. C. Glazer, *J. Am. Chem. Soc.*, 2012, **134**, 8324–8327.

6 K. Kalyanasundaram and M. Grätzel, *Coord. Chem. Rev.*, 1998, **177**, 347–414.

7 S. B. Beil, S. Bonnet, C. Casadevall, R. J. Detz, F. Eisenreich, S. D. Glover, C. Kerzig, L. Naesborg, S. Pullen, G. Storch, N. Wei and C. Zeymer, *JACS Au*, 2024, **4**, 2746–2766.

8 S. Das, C. D. Zhu, D. Demirbas, E. Bill, C. K. De and B. List, *Science*, 2023, **379**, 494–499.

9 G. E. M. Crisenza and P. Melchiorre, *Nat. Commun.*, 2020, **11**, 803–806.

10 N. A. Romero and D. A. Nicewicz, *Chem. Rev.*, 2016, **116**, 10075–10166.

11 J. L. Lilly, G. Romero, W. J. Xu, H. Y. Shin and B. J. Berron, *Biomacromolecules*, 2015, **16**, 541–549.

12 J. Niu, D. J. Lunn, A. Pusuluri, J. I. Yoo, M. A. O'Malley, S. Mitragotri, H. T. Soh and C. J. Hawker, *Nat. Chem.*, 2017, **9**, 537–545.

13 P. P. Singh, S. Sinha, P. Gahtori, D. N. Mishra, G. Pandey and V. Srivastava, *Dyes Pigm.*, 2024, **229**, 112262.

14 Z. Z. Zheng, D. Eglin, M. Alini, G. R. Richards, L. Qin and Y. X. Lai, *Engineering*, 2021, **7**, 966–978.

15 J. Geng, W. S. Li, Y. C. Zhang, N. Thottappillil, J. Clavadetscher, A. Lilienkampf and M. Bradley, *Nat. Chem.*, 2019, **11**, 578–586.

16 B. Pfund and O. S. Wenger, *JACS Au*, 2025, **5**, 426–447.

17 G. Kumar, B. Cai, S. Ott and H. Tian, *Chem. Phys. Rev.*, 2023, **4**, 011307.

18 N. Méndez-Gil, S. Gámez-Valenzuela, M. Echeverri, G. H. Suyo, M. Iglesias, M. C. R. Delgado and B. Gómez-Lor, *Adv. Funct. Mater.*, 2024, **34**, 2316754.

19 Z. Bao and J. Locklin, *Organic field-effect transistors*, CRC Press, Boca Raton, 2007.

20 P. van der Scheer, T. van de Laar and J. Sprakel, *Sci. Rep.*, 2019, **9**, 11217.

21 D. Aguilar-Ferrer, J. Szewczyk and E. Coy, *Catal. Today*, 2022, **397**, 316–349.

22 H. Lee, S. M. Dellatore, W. M. Miller and P. B. Messersmith, *Science*, 2007, **318**, 426–430.

23 C. G. Bailey, M. D. Nothling, L. L. Fillbrook, Y. Vo, J. E. Beves, D. R. McCamey and M. H. Stenzel, *Angew. Chem., Int. Ed.*, 2023, **62**, e202301678.

24 A. B. Mostert, S. B. Rienecker, C. Noble, G. R. Hanson and P. Meredith, *Sci. Adv.*, 2018, **4**, eaaq1293.

25 L. Panzella, G. Gentile, G. D'Errico, N. F. Della Vecchia, M. E. Errico, A. Napolitano, C. Carfagna and M. d'Ischia, *Angew. Chem., Int. Ed.*, 2013, **52**, 12684–12687.

26 A. Menichetti, D. Mordini and M. Montalti, *Chem.–Eur. J.*, 2024, **30**, e202400461.

27 C. Russo, F. Brunelli, G. C. Tron and M. Giustiniano, *J. Org. Chem.*, 2023, **88**, 6284–6293.

28 Y. M. Tian, W. Silva, R. M. Gschwind and B. König, *Science*, 2024, **383**, 750–756.

29 C. Y. Wu, N. Corrigan, C. H. Lim, W. J. Liu, G. Miyake and C. Boyer, *Chem. Rev.*, 2022, **122**, 5476–5518.

30 H. Kim, Y. J. Jung and J. K. Lee, *Polym. Chem.*, 2021, **12**, 970–974.

31 H. Ko, Y. J. Jung, M. Kim, H. Kim, D. Lee, R. Kim, W. O. Choi, H.-I. Lee and J. K. Lee, *Dyes Pigm.*, 2024, **226**, 112152.

32 J. B. Nganga, Y. J. Jung, Y. Si, M. Kim, H. Ko, G. T. Hwang, H. J. Lee, H.-I. Lee and J. K. Lee, *Dyes Pigm.*, 2022, **200**, 110163.

33 J. Y. Kim, B. S. Lee, J. Choi, B. J. Kim, J. Y. Choi, S. M. Kang, S. H. Yang and I. S. Choi, *Angew. Chem., Int. Ed.*, 2016, **55**, 15306–15309.

34 D. J. Siegwart, J. K. Oh and K. Matyjaszewski, *Prog. Polym. Sci.*, 2012, **37**, 18–37.

35 W. X. Cheng, F. F. Fan, Y. Zhang, Z. C. Pei, W. J. Wang and Y. X. Pei, *Polymers*, 2017, **9**, 135.

36 R. Mrówczynski, L. E. Coy, B. Scheibe, T. Czechowski, M. Augustyniak-Jablokow, S. Jurga and K. Tadyszak, *J. Phys. Chem. B*, 2015, **119**, 10341–10347.

37 J. Liebscher, R. Mrówczynski, H. A. Scheidt, C. Flip, N. D. Hadade, R. Turcu, A. Bende and S. Beck, *Langmuir*, 2013, **29**, 10539–10548.

38 H. A. Lee, E. Park and H. Lee, *Adv. Mater.*, 2020, **32**, 1907505.

39 H. Hemmatpour, O. De Luca, D. Crestani, M. C. A. Stuart, A. Lasorsa, P. C. A. van der Wel, K. Loos, T. Giousis, V. Haddadi-Asl and P. Rudolf, *Nat. Commun.*, 2023, **14**, 664.

40 N. J. Hestand and F. C. Spano, *Chem. Rev.*, 2018, **118**, 7069–7163.

41 Y. H. Deng, W. Yuan, Z. Jia and G. Liu, *J. Phys. Chem. B*, 2014, **118**, 14536–14545.

42 J. F. Hu, L. Yang, P. Yang, S. H. Jiang, X. H. Liu and Y. W. Li, *Biomater. Sci.*, 2020, **8**, 4940–4950.

43 A. Aguirre-Soto, K. Kaastrup, S. Kim, K. Ugo-Beke and H. D. Sikes, *ACS Catal.*, 2018, **8**, 6394–6400.

44 D. Lee, M. Park, N. Kim, M. Gu, H. I. Kim and B. S. Kim, *J. Catal.*, 2022, **411**, 235–244.

45 S. E. Braslavsky, *Pure Appl. Chem.*, 2007, **79**, 293–465.

46 W. O. Choi, Y. J. Jung, M. Kim, H. Kim, J. J. Li, H. Y. B. Ko, H.-I. Lee, H. J. Lee and J. K. Lee, *ACS Omega*, 2023, **8**, 40277–40286.

47 H. J. Avens and C. N. Bowman, *J. Polym. Sci., Part A: Polym. Chem.*, 2009, **47**, 6083–6094.

48 S. Matsuoka, T. Kikuno, K. Takagi and M. Suzuki, *Polym. J.*, 2010, **42**, 368–374.

49 A. M. Brugh and M. D. E. Forbes, *Chem. Sci.*, 2020, **11**, 6268–6274.

50 J. V. Paulin, A. Batagin-Neto, B. Naydenov, K. Lips and C. F. O. Graeff, *Mater. Adv.*, 2021, **2**, 6297–6305.

51 M. D. Nothling, C. G. Bailey, L. L. Fillbrook, G. N. Wang, Y. J. Gao, D. R. McCamey, M. Monfared, S. Wong, J. E. Beves and M. H. Stenzel, *J. Am. Chem. Soc.*, 2022, **144**, 6992–7000.

52 M. Pinteala and S. Schlick, *Polym. Degrad. Stab.*, 2009, **94**, 1779–1787.

53 P. Bilski, K. Reszka, M. Bilska and C. F. Chignell, *J. Am. Chem. Soc.*, 1996, **118**, 1330–1338.

54 H. Bader, V. Sturzenegger and J. Hoigné, *Water Res.*, 1988, **22**, 1109–1115.

55 K. M. Schaich and D. C. Borg, *Lipids*, 1988, **23**, 570–579.

56 L. Eberson, *J. Chem. Soc., Perkin Trans. 2*, 1994, 171–176.

57 B. Kalyanaraman, C. Mottley and R. P. Mason, *J. Biochem. Biophys. Methods*, 1984, **9**, 27–31.

58 D. L. Haire, U. M. Oehler, P. H. Krygsman and E. G. Janzen, *J. Org. Chem.*, 1988, **53**, 4535–4542.

59 K. Reszka and C. F. Chignell, *Photochem. Photobiol.*, 1983, **38**, 281–291.

60 M. J. Turner, D. B. Everman, S. P. Ellington and C. E. Fields, *Free Radical Biol. Med.*, 1990, **9**, 415–421.

61 M. J. Turner, C. H. Bozarth and K. E. Strauss, *Biochem. Pharmacol.*, 1989, **38**, 85–90.

62 M. K. Eberhardt and R. Colina, *J. Org. Chem.*, 1988, **53**, 1071–1074.

63 D. H. Chin, G. Chiericato, E. J. Nanni and D. T. Sawyer, *J. Am. Chem. Soc.*, 1982, **104**, 1296–1299.

64 C. C. Felix, J. S. Hyde and R. C. Sealy, *Biochem. Biophys. Res. Commun.*, 1979, **88**, 456–461.

65 X. Chen, Z. F. Liu and W. J. Jin, *J. Phys. Chem. A*, 2020, **124**, 2746–2754.

66 Y. N. Lee, J. Kim, S. H. Y. Lee, E. Sim and J.-I. Hong, *Chem. Eng. J.*, 2023, **476**, 146659–146665.

67 P. Meredith and T. Sarna, *Pigm. Cell Res.*, 2006, **19**, 572–594.